

Statistical Downscaling of Gridded Wind Speed Data Using Local Topography

ADAM WINSTRAL, TOBIAS JONAS, AND NORA HELBIG

WSL-SLF, Davos Dorf, Switzerland

(Manuscript received 11 March 2016, in final form 2 November 2016)

ABSTRACT

Winds, particularly high winds, strongly affect snowmelt and snow redistribution. High winds during rain-on-snow events can lead to catastrophic flooding while strong redistribution events in mountain environments can generate dangerous avalanche conditions. To provide adequate warnings, accurate wind data are required. Yet, mountain wind fields exhibit a high degree of heterogeneity at small spatial lengths that are not resolved by currently available gridded forecast data. Wind data from over 200 stations across Switzerland were used to evaluate two forecast surface wind products (~2- and 7-km horizontal resolution) and develop a statistical downscaling technique to capture these finer-scaled heterogeneities. Wind exposure metrics derived from a 25-m horizontal resolution digital elevation model effectively segregated high, moderate, and low wind speed sites. Forecast performance was markedly compromised and biased low at the exposed sites and biased high at the sheltered, valley sites. It was also found that the variability of predicted wind speeds at these sites did not accurately represent the observed variability. A novel optimization scheme that accounted for local terrain structure while also nudging the forecasted distributions to better match the observed distributions and variability was developed. The resultant statistical downscaling technique notably decreased biases across a range of elevations and exposures and provided a better match to observed wind speed distributions.

1. Introduction

Wind fields are extremely complex. Dynamic, nonlinear flow at very short time scales challenges the capabilities of numerical modeling solutions (Wood 2000). Numerical models are computationally demanding, and even carefully conducted laboratory studies of these nonlinear phenomena are prone to difficulties and uncertainties (Harindra and Sermal 2012; Stuart 2012). Forecasted wind fields, most often derived from regional- to global-scaled weather models, entail further uncertainties related to defining boundary conditions and capturing terrain interactions. Furthermore, in mountain regions with complex topography, winds exhibit large variability at spatial lengths far smaller than can be resolved by current forecast models (e.g., Raderschall et al. 2008; Winstral et al. 2009). Yet, these finer-scaled heterogeneities are vitally important to determining melt rates in rain-on-snow (RoS) events (Marks et al. 1998; Würzer et al. 2016) and snow

redistribution (Lehning et al. 2008; Liston and Sturm 1998; Mott et al. 2011; Pomeroy et al. 1993).

RoS floods are capable of causing extensive damage, posing risks to both infrastructure and life (Kattlemann 1997; Marks et al. 1998; Pomeroy et al. 2016). As the climate warms, RoS floods are changing in nature, with increasing prevalence in places typically not prone to such events (Freudiger et al. 2014; Surfleet and Tullos 2013). Wind-driven turbulent energy fluxes between the atmosphere and snow surface often drive the high melt rates experienced in RoS floods (Kattlemann 1997; Marks et al. 1998). Water leaving the snowpack during these events is additionally dependent on snow states such as depth and energy content (Wever et al. 2014; Würzer et al. 2016). Distributed mass- and energy-balance snow models explicitly calculate energy and mass fluxes while tracking snow states and have outperformed conceptual snowmelt models during RoS events (Kumar et al. 2013). With recent advances in computing capabilities, these comprehensive snow models are increasingly being used for operational purposes (e.g., Painter et al. 2016). The potential to accurately forecast snowmelt contributions to RoS events is now possible. However, achieving this is directly

Corresponding author e-mail: Adam Winstral, adam.winstral@slf.ch

dependent on having accurate forcing data, of which development of efficient means of downscaling forecasted wind data is a vital component. Though there are many associated benefits of the presented work, it is driven by the need to improve operational snowmelt runoff forecasts.

Based on the importance of temperature and precipitation in many modeling applications, and perhaps partly because their heterogeneity can be reasonably described by physical principles, downscaling of temperature and precipitation data have been the subject of numerous studies (e.g., [Daly et al. 2008](#); [Gao et al. 2012](#); [Running et al. 1987](#)). Wind fields, however, are far more complex; their significance is often limited to specific applications, events, and regions and have been the subject of far fewer downscaling studies.

Downscaling is often classified into two classes: dynamic and nondynamic. Dynamic approaches apply concepts similar to those present in the original models but do so at higher resolutions (e.g., nested modeling). Nondynamic approaches can be based on physical principles linking the low-resolution forecasts to higher-resolution data (e.g., low-resolution forecasted air temperatures and lapse rates applied to higher-resolution elevation data) or on derived statistical relationships (e.g., the relationship between forecast climate variables and finer-scaled observations or products). The two nondynamic approaches as described here are often grouped together as “statistical” solutions ([Benestad et al. 2008](#)). The nondynamic solutions have far lower computational demands and can potentially account for forecast biases using data and methods extrinsic to the forecasting model(s). For these reasons, nondynamical approaches remain a practical choice for operational purposes.

Nondynamic wind downscaling studies have focused on improving point realizations and deriving higher-resolution raster products of either probability density functions or wind speed estimates. Wind speed distributions are important for estimating potential wind energy production and for developing construction codes and assessing potential damages associated with high winds. [Kirchmeier et al. \(2014\)](#) used statistical downscaling to estimate daily probability density functions at 31 stations in the north-central United States from National Centers for Environmental Prediction–National Center for Atmospheric Research (NCEP–NCAR) reanalyses data (~200 km resolution), while [Curry et al. \(2012\)](#) sought statistical relationships between climate forecast variables and similar reanalysis data to derive monthly Weibull distribution parameters. [Huang et al. \(2015\)](#) used a combination of physical and statistical nondynamic downscaling techniques to test

if a high-resolution (3 km) product similar to the dynamically derived Weather Research and Forecasting (WRF) Model could be more efficiently produced from the North American Regional Reanalysis (NARR) model (~32 km resolution). Differences in roughness lengths between the NARR and WRF products as well as NARR-predicted surface conditions were used in the downscaling scheme. The authors noted that performance did degrade over highly complex terrain. [De Rooy and Kok \(2004\)](#) used a similar conceptual framework based on low- and high-resolution roughness depictions and a generalized additive model (GAM) to downscale the High Resolution Limited Area Model (HIRLAM; ~75 km resolution) to six stations in the Netherlands.

Of greater relevancy to this work is research focused on downscaling forecast winds to estimate wind speeds or dynamics at stations in varied terrain, including mountain sites. [Salameh et al. \(2009\)](#), similar to [de Rooy and Kok \(2004\)](#), used a GAM and ERA-40 variables to develop site-specific regressions to predict vector wind components at six sites in southern France. [Trubilowicz et al. \(2016\)](#) used vertical and horizontal interpolations to downscale NARR free-atmosphere meteorological predictions to observations at three ridge-top sites in southwestern Canada, concluding that debiasing techniques could further improve upon their results.

[Fiddes and Gruber \(2014\)](#) and [Etienne et al. \(2010\)](#) both presented research using many of the same stations used in the current work. [Fiddes and Gruber \(2014\)](#) developed the TopoSCALE application to downscale meteorological data to 40 Swiss Federal Office of Meteorology and Climatology (MeteoSwiss) Autotelefon-Netz (ANETZ) and 159 Intercantonal Measurement and Information System (IMIS) observation stations in Switzerland. The TopoSCALE wind technique interpolated pressure-level, free-air wind speeds from ERA-Interim (~80 km) using estimates of station pressure-level elevations. They found that surface-level predicted wind speeds were biased low compared to observations and that the TopoSCALE-adjusted free-air wind speeds substantially improved simulations of mean daily wind speeds. They also tested a topography-based wind submodel ([Liston and Sturm 1998](#)); however, analysis of the submodel was limited (results from only one station reported) because of difficulties in accurately assessing local station conditions. [Etienne et al. \(2010\)](#) did not perform downscaling but did use topographic analysis at 70 ANETZ stations in Switzerland to build a spatial model of 98th percentile daily maximum wind speeds. They used two terrain parameters, termed topographic position indices (TPIs; [Jenness 2006](#); [Weiss 2001](#)), along with slope to classify landforms. Though

statistical model selection criteria consistently removed the landform predictor from their wind model, the authors forced its inclusion based on landform being “the most influential parameter on the wind flow” (Etienne et al. 2010, p. 1962).

Winstral et al. (2009), by contrast, found a significant relationship between a terrain parameter (S_x) and wind speed differences. They showed that wind speed heterogeneity across varied terrain could be approximated at high resolution using this simply derived terrain parameter. The terrain parameter (i.e., S_x) is a direction-dependent, slope-based assessment of topographic shelter and exposure that has been used to distribute hourly observed wind speeds across a modeling domain (Kumar et al. 2013; Marks et al. 2002; Winstral et al. 2014). The S_x and other terrain variables have also been shown to adequately delineate areas of high and low wind speeds to parameterize the effects of wind-induced snow redistribution (Anderton et al. 2004; Erickson et al. 2005; Purves et al. 1998; Schirmer et al. 2011; Winstral et al. 2013). The challenge confronted in the current work—capturing subgrid features from a single forecasted cell—has many similarities to those encountered in distributing a single measurement across varied terrain.

The overriding goal of this study was to improve spatial snow modeling capabilities through improved depictions of mountain winds. Because of the high spatiotemporal heterogeneity of mountain winds and the strong dependencies of RoS melt and snow redistribution to wind speed, the current research is conducted at high spatial (from point to 25-m horizontal resolutions) and temporal resolutions (1 h). Our hypothesis is that high-resolution terrain data in conjunction with wind observations collected at various elevations and exposures can be used to statistically downscale low-resolution wind forecasts to better capture the mean effects of local topography on mountain winds. As such, this research looks to fill several important gaps in the currently available research and differs from most, if not all, prior downscaling efforts in many ways:

- 1) Whereas most studies have focused on low-wind sites at low to midelevations, or contained only a few high-wind mountain observations (e.g., Huang et al. 2015; Jiménez and Dudhia 2012; Trubilowicz et al. 2016; Žagar et al. 2006), this study includes a large set of high-wind, exposed mountain sites. Only Fiddes and Gruber (2014) included a large set of high-wind mountain sites in their analysis. These sites were, however, incorporated into a larger dataset in the main analysis, and application of the high-resolution, topographic-based submodel was inconclusive. The

present research includes many of these same sites, but given the importance of high winds to this work and the vast terrain effects on wind, location-specific tendencies and local topography are extensively assessed.

- 2) Roughness lengths (de Rooy and Kok 2004; Huang et al. 2015) and a general-purpose landform characterization (Etienne et al. 2010) have been used as high-resolution descriptors of local topography, but these measures are not direction dependent and cannot differentiate leeward and windward positions. This work considers S_x , a proven, wind-specific terrain parameterization capable of differentiating such slopes based on given wind directions.
- 3) Many of the prior studies developed station-specific corrections (e.g., Kirchmeier et al. 2014; Salameh et al. 2009). However, these types of corrections have limited spatial capabilities. The procedures applied in this research were not station specific to facilitate spatial applications.
- 4) Most of the earlier work has focused on multihour to daily mean winds (e.g., Fiddes and Gruber 2014; Huang et al. 2015; Jiménez and Dudhia 2012; Salameh et al. 2009). While Horvath et al. (2012) used hourly winds to assess a dynamically downscaled product's (WRF) ability to reproduce diurnal wind patterns, the highest-resolution product had a grid scale of 333 m, and only four high-wind sites were included in the study.
- 5) The stationarity of the developed procedures will be tested using an independent validation period, whereas the aforementioned nondynamic/statistical applications have focused on calibration results.
- 6) Additionally, many of these prior works assessed and downscaled comparatively low-resolution forecast data. While many of these earlier methodologies are compatible with higher-resolution forecast data, the forecast data analyzed and applied in this study are of far higher resolutions (~ 2 - and ~ 7 -km horizontal resolutions) than many of the prior analyses. These higher-resolution weather products are rapidly becoming standard tools for mountain applications [e.g., WRF, High-Resolution Rapid Refresh (HRRR), and Consortium for Small-Scale Modeling (COSMO)].

2. Data

Essentially, 2 years of wind data were assessed in this study. Given the snow-oriented focus that prompted this research, data from July through September were not included in the analysis. Initial data analysis and model

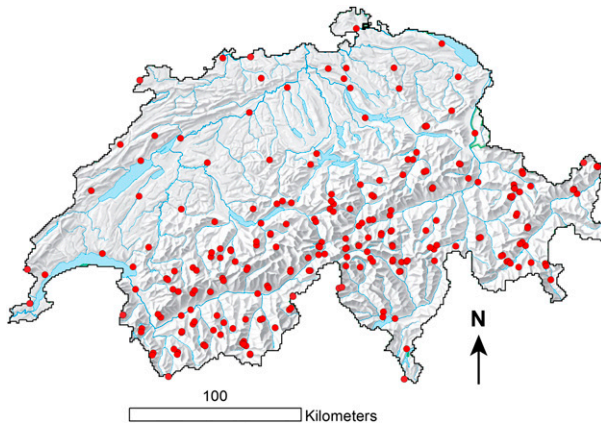


FIG. 1. Distribution of observation sites.

calibration were performed on data spanning from 1 October 2014 through 30 June 2015. Data from 1 October 2013 through 30 June 2014 were set aside for validating the results.

The COSMO model is a nonhydrostatic, limited-area atmospheric prediction model (www.cosmo-model.org). COSMO forecast products are used in operational applications throughout Switzerland by agencies including MeteoSwiss; the Swiss Federal Office for the Environment; and the Swiss Federal Institute for Forest, Snow and Landscape Research (WSL) Institute for Snow and Avalanche Research (SLF). The high-resolution COSMO-2 model (~ 2.2 -km resolution) is focused primarily on the European Alps to provide improved forecasts of the rugged region. COSMO-7 (~ 6.6 -km resolution) covers all of western and central Europe. Both models have 60 vertical layers. COSMO-2 and COSMO-7 products are updated several times a day with forecast lead times of 33–45 h (COSMO-2) and 72 h (COSMO-7). The COSMO data available for this study consist of 10-m surface wind vector forecasts at hourly resolution. Continuous time series were assembled from at least one forecast per day (0900 UTC run for COSMO-2 and 1200 UTC run for COSMO-7), so that the maximum lead time for any given time step was 24 h.

Hourly averaged wind observations used in this study were from automated stations in the SwissMetNet (65 stations) and IMIS (154 stations) observation networks and provide spatial coverage across all of Switzerland (Fig. 1). The SwissMetNet stations are operated and maintained by MeteoSwiss, while the IMIS stations are operated by SLF. The SwissMetNet stations used in this study vary in elevation from 197 to 3580 m MSL and have a median elevation of 779 m MSL, a 1-s sampling rate, and a 10-m instrument height. The IMIS network is primarily used for avalanche forecasting and features a

denser network of high-elevation sites. IMIS sites often feature pairs or triplets of stations in wind-exposed and wind-sheltered locations designed to accurately assess wind and snow conditions and their local variability. IMIS stations used in this study vary in elevation from 1560 to 3345 m MSL and have a median elevation of 2455 m MSL, a 5-s sampling rate, and a 6.5-m instrument height. To ensure compatibility, IMIS data were adjusted to match the instrument height of the SwissMetNet stations using a standard log wind profile (Stull 1988) with a roughness length of 0.005 m. Taken together, these stations capture a wide range of elevations, topographic positions, and wind environments. Mean station wind speeds during the calibration period varied from 0.6 to 8.6 ms^{-1} . Only time steps where observed wind speeds were greater than 0.2 ms^{-1} were included in the analysis.

3. Methods

In the first analysis step, relationships between forecast data and observations during the calibration period were examined (section 4a). The COSMO forecast data used in these evaluations came directly from the COSMO pixel containing each station. Where relevant, relationships between forecast biases and high-resolution topographic structure not resolved by the lower-resolution forecasts were evaluated. To facilitate potential spatial applications using these methods, overall trends in these data were pursued as opposed to station-specific analyses. The primary tools of analysis were two standard statistical metrics—root-mean-square error (RMSE) and mean bias error (MBE)—and the Kolmogorov–Smirnov D statistic (KSD). The KSD quantifies the degree to which two distributions match with $D = 0$, indicating a perfect match. While these initial investigations focused on the calibration dataset, some of the provided examples will demonstrate corresponding trends taken from the validation dataset. The validation data are shown to facilitate subsequent comparisons used for model validation.

Subgrid or high-resolution topographic structure at each station was determined from a 25-m-resolution digital elevation model (DEM) using two established metrics: the TPI (Jenness 2006; Weiss 2001) and S_x , a slope-based, direction-dependent parameter that describes the upwind topography at each location (Winstral et al. 2002, 2009). Both of these indices are easily derived from DEMs thereby fully supporting spatial applications.

The TPI provides a broad description of each station's elevation relative to its surroundings and is not direction dependent. TPIs in this derivation consisted of each

station's 25-m DEM elevation minus the mean of all pixel elevations located within a 2-km radius of the station. The Sx algorithm examines all cells along a fixed search line emanating from the cell of interest (e.g., grid

cell containing each station) to determine which cell has the greatest upward slope relative to the cell of interest. Once found, the algorithm returns the value of this slope in degrees:

$$Sx_{A,d_{\max}}(x_i, y_i) = \max \left(\tan^{-1} \left\{ \frac{\text{ELEV}(x_v, y_v) - [\text{ELEV}(x_i, y_i) + \text{height}]}{[(x_v - x_i)^2 + (y_v - y_i)^2]^{0.5}} \right\} \right), \quad (1)$$

where A is the azimuth of the search direction, d_{\max} determines the lateral extent of the search, (x_i, y_i) are the coordinates of the cell of interest, and (x_v, y_v) are the set of all cell coordinates located along the line segment defined by (x_i, y_i) , A , and d_{\max} . The height parameter, in the same unit as elevation, was initially introduced to account for instrument heights (Winstral et al. 2009) and was also found to reduce the impact of small proximal, terrain perturbations on Sx derivations (Winstral et al. 2013). Positive Sx values indicate sheltering features whose elevation exceeds that of the cell of interest plus the additional height. Negative Sx values indicate that the cell of interest including the additional height is the highest cell along the search line and is topographically exposed. The d_{\max} variable controls the extent of terrain included in the analysis and can have a substantial effect on Sx (Winstral and Marks 2002; Winstral et al. 2009). Similar to prior applications, Sx values were derived at 5° increments within 30° upwind windows centered on each increment. Hourly station-observed wind directions were rounded to the nearest 5° with direction-appropriate Sx values registered to the observations. Three different d_{\max} derivations of Sx, all with 8 m height, were applied to test for near and far terrain influences on forecasted and station-observed wind speed differences: 300 m (Sx-300), 500 m (Sx-500*), and 2 km (Sx-2k*). In the case of Sx-500* and Sx-2k*, the search did not include the nearest 100 m of terrain, but rather the search began 100 m upwind of the site location. This was done as a means of compensating for potential inaccuracies in station locations (cf. Fiddes and Gruber 2014). For example, if a site is located on a peak, Sx should indicate that this site is exposed to all directions. If, however, the station coordinates contain some error, the station will be placed on a slope leading to the peak and the Sx derivations will indicate the site is sheltered relative to some wind directions. In these instances, excluding the nearest 100-m of terrain should reduce the sensitivity of Sx to location inaccuracies.

An extensive calibration period analysis addressed several aspects of the relationship between COSMO-predicted and observed wind speeds. Both spatial and temporal dependencies were investigated. Comparisons

between the distributions of forecasted wind speeds and observations were also made. Based on these assessments a statistical downscaling technique was formulated to simultaneously reduce MBE, RMSE, and KSD between forecasted and observed wind speeds (section 4b). To achieve this, regression models of observed biases during the calibration period were developed with a customized optimization. The modeled biases were then subtracted from the forecasted wind speeds to produce the downscaled speeds.

The key to achieving the multiple objectives was the adaptable optim function in the R software package (R Development Core Team 2015). Optim is a general-purpose optimization routine based on the Nelder–Mead method (Nelder and Mead 1965) that allows the user to design optimization criteria. Optimization was based on minimizing the weighted sum of ordinary least squares, which incorporates bias reduction, and the KSD. Relative weighting of these two independent measures that varied by an order of magnitude was iterative and subjective. Weights were adjusted, with the main objective being bias removal and improved depictions of the high-wind component critical to snow modeling. Hence, bias reduction and minimizing the KSD statistic were the primary considerations in assigning weights. RMSE reduction was of secondary importance, with the general stipulation that RMSE in the downscaled model remains close to or lower than the uncorrected values. Further details on the downscaling derivation and the optimization routine are provided in section 4b subsequent to the forecast data assessments.

The validation dataset runs from 1 October 2013 through 30 June 2014. The point validation results are presented in section 4c, followed by an example spatial application in section 4d. Compared to trends in the subsequent time periods, the COSMO-7 data prior to mid-January 2014 displayed marked differences in its relationship to both observations and the COSMO-2 data. Whether this was related to changes inherent to the COSMO-7 forecast data could not be determined. Nevertheless, the validation period for the COSMO-7 downscaling was limited to the February–June period.

TABLE 1. Summary statistics of the relationship between nearest-neighbor COSMO-predicted and station-observed wind speeds. The 1-h results are for hourly comparisons, and the 6-h results represent results of 6-h averaged values. Validation period for COSMO-7 is from February to June.

	COSMO-2			COSMO-7		
	Calibration (1 h)	Calibration (6 h)	Validation (1 h)	Calibration (1 h)	Calibration (6 h)	Validation (1 h)
RMSE (m s^{-1})						
Overall	2.60	2.31	2.50	2.65	2.41	2.37
Valleys	2.17	1.88	2.04	2.01	1.77	1.83
Upper slopes	2.97	2.66	2.84	3.18	2.93	2.78
Ridges	3.53	3.22	3.59	3.84	3.59	3.43
MBE (m s^{-1})						
Overall	-0.21	-0.18	-0.29	-0.30	-0.27	-0.31
Valleys	0.50	0.52	0.42	0.54	0.55	0.35
Upper slopes	-0.99	-0.92	-1.02	-1.22	-1.15	-0.99
Ridges	-1.92	-1.89	-2.01	-2.28	-2.25	-1.84
KSD (unitless)						
Overall	0.04	0.05	0.05	0.10	0.09	0.09
Valleys	0.12	0.11	0.12	0.20	0.18	0.17
Upper slopes	0.16	0.16	0.16	0.20	0.20	0.18
Ridges	0.30	0.32	0.31	0.36	0.38	0.31

4. Results and discussion

a. COSMO forecast analysis

Comparisons between hourly nearest-gridcell forecasted wind speeds and observations had a lot of scatter [Table 1, Calibration (1 h)]. During the calibration year, RMSEs (percent of observed mean) for the COSMO-2 and COSMO-7 products were 2.60 m s^{-1} (87%) and 2.65 m s^{-1} (88%), respectively. Both forecast products had tendencies to overpredict low observations and underpredict high observations. This pattern was more obvious in the COSMO-7 product (Fig. 2). Overall, COSMO-2 (-0.21 m s^{-1}) and COSMO-7 (-0.30 m s^{-1}) underpredicted wind speeds across the observational network. These overall biases, however, may not be representative of the COSMO performance but more a reflection of the stations used in this analysis. Most of the observations are from mountain locations where wind speeds are expected to be greater than those at lower elevations. Given the conservative tendencies of the forecast products, the observed negative biases were not unexpected. The validation period [Table 1, Validation (1 h)] produced similar results to those detailed above for the calibration period.

Biases were related to terrain position. Figure 3 shows biases binned by TPI (also Table 1). Negative biases were prominent at stations located 200 m higher than the proximal mean 2-km elevation (i.e., $\text{TPI} > 200 \text{ m}$), and positive biases were prominent at $\text{TPI} \leq 200 \text{ m}$. The magnitude of negative biases increased with increasing relative exposure. Though the $\text{TPI} \leq 200 \text{ m}$ bins all had positive biases, the magnitude of biases was not

correlated to TPI as they were for $\text{TPI} > 200 \text{ m}$. In the underpredicted bins, the magnitudes of COSMO-7 biases were consistently higher than the COSMO-2 biases. A similar trend was not apparent in the overpredicted bins. Analogous terrain-related biases could be segregated using any of the other tested terrain variables (S_x). The directional independency of TPI, however, has a

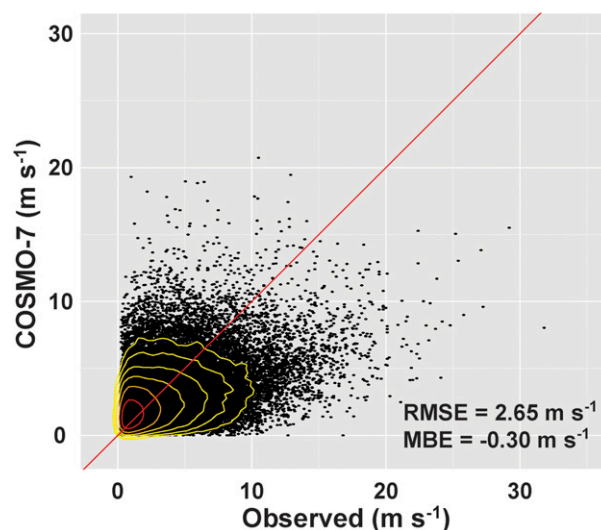


FIG. 2. Scatterplot of nearest-neighbor COSMO-7-predicted and station-observed wind speeds during the calibration period (only 5% of the $>1.14 \times 10^6$ data points plotted). The contours are two-dimensional kernel density estimates reflecting equal occurrence probabilities. The vertical nature of the innermost contours indicates the tendency to overpredict low wind speeds, whereas the flatter outer contours indicate the tendency to underpredict high winds.

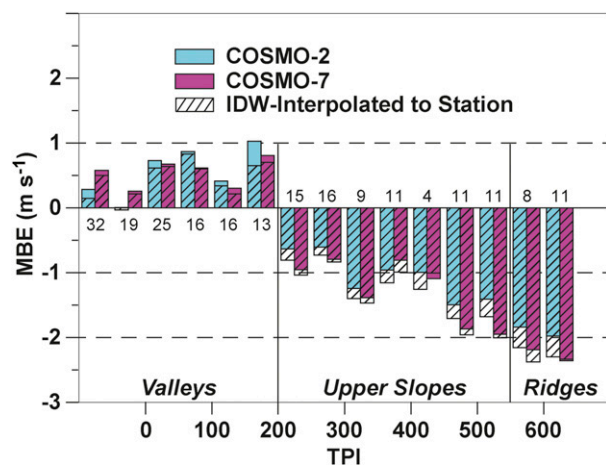


FIG. 3. MBEs binned by TPI for both the COSMO-2 and COSMO-7 products during the calibration period. The solid bars represent results using COSMO nearest neighbors; the hatched bars are the results from inverse-squared distance-weighted interpolations from the COSMO cell centers to the station coordinates. The numbers at the base of the bars indicate how many observation sites were in each bin.

considerably lower computational cost than the direction-dependent solutions.

Based on trends apparent in Fig. 3, the stations were parsed into three topographic groups. The $TPI \leq 200$ bins all had positive average biases, yet a physically plausible trend with TPI was not evident. These TPI values are representative of lower slope to valley locations and will be referred to as “valleys.” For $200 < TPI \leq 550$, all biases were negative, with the magnitude of biases seemingly increasing with increasing TPI. These locations are relatively exposed and will be referred to as “upper slopes.” Stations with $TPI > 550$ are in locations considerably higher than the surrounding terrain and had the strongest biases. This latter group will be referred to as “ridges.” As expected, observed wind speeds were greatest at the ridges, decreased at upper slopes, and were lowest in the valleys (Table 2). By contrast, though the COSMO-2 data exhibited some of the observed wind speed differences between the valley and upper slope locations, these data were incapable of further resolving the more exposed ridge locations. The COSMO-7 data struggled to differentiate any wind speed differences between these topological groups. Though the TPI split of the upper slope and ridge groups was somewhat arbitrary, it was done with the intention of segregating and separately addressing the strong biases at these high-wind sites that the forecast data could not resolve. These observations underscore the need for developing improved methods of downscaling and debiasing low-resolution wind data in complex terrain.

TABLE 2. Average wind speeds (m s^{-1}) grouped by TPI classes during the calibration period.

	Observed	COSMO-2	COSMO-7
Valleys	2.18	2.68	2.72
Upper slopes	3.94	2.96	2.73
Ridges	4.89	2.97	2.61

Oftentimes, gridded data are transferred to stations using spatial interpolation methods, whereas the aforementioned results were the product of taking data from the nearest grid cell. Figure 3 also plots inverse-squared distance-weighted interpolations from the COSMO gridcell centers to the station coordinates along with the nearest-gridcell results. At the underpredicted, ridge-type sites, the interpolations further decreased forecasted wind speeds and degraded performance. The spatial interpolation, however, improved results at the valley locations. Without a clear-cut advantage to either method, given that the main goal of this project was improving snow simulations where high wind speeds can contribute substantially to melt rates in RoS events and the redistribution of snow, the nearest-gridcell method was adopted for the foregoing analysis. Prior downscaling and debiasing wind studies have similarly used a nearest-neighbor approach (e.g., de Rooy and Kok 2004; Huang et al. 2015; Abatzoglou 2013).

Time step sensitivity was also assessed. Six-hour running averages of forecast and station data were derived. Evaluation was limited to 6-h periods without data gaps. Summary results can be found in Table 1 under the heading “Calibration (6h).” While RMSEs for both the COSMO-2 and COSMO-7 forecast data were reduced by $\sim 10\%$, bias changes due to the time averaging were less than 0.05 m s^{-1} . The time-averaged reduction in RMSEs was expected and has been seen in other studies as well (e.g., Fiddes and Gruber 2014). These results, however, do indicate that biases present in the forecast data are not related to timing differences and are largely due to subgrid topographic structures not resolved in the forecast data.

An assessment of model and observed winds indicated that there was also a seasonal component in errors (Fig. 4). Errors, expressed as percentages of the monthly mean forecasted winds, exhibited a similar trend. Fiddes and Gruber (2014) similarly found a seasonal trend in forecast (ERA-Interim) bias at many of these same sites. On upper slopes and ridges, errors were largest in December and January and decreased toward the summer months. The magnitude of errors in the valley locations were also lower in spring tending toward summer, but this trend was not as strong as exhibited at the more exposed locations. Similar trends were also apparent for the COSMO-7 data and for both products

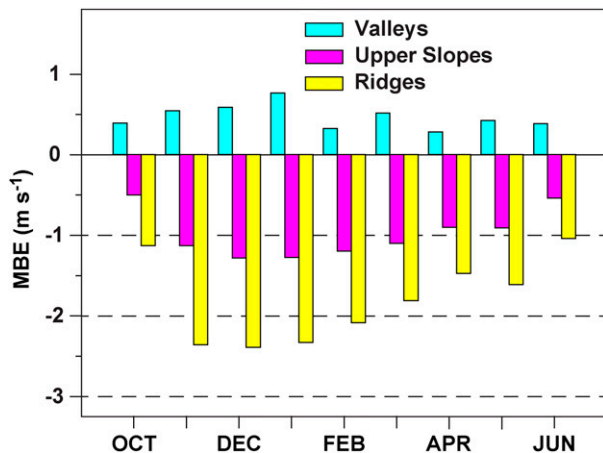


FIG. 4. MBEs distributed by month during the calibration period for the COSMO-2 data. The magnitude of errors was greatest during the November–January period and lowest during the early spring. Similar patterns were found in the COSMO-7 data and in both products during the validation period.

during the validation period (not shown). The seasonality could in part be due to differences in synoptic weather patterns, wind speed magnitudes, vegetation growth, or a combination of these.

Diurnal wind patterns were not evident at the stations or in the forecast data during the November–January period but did become evident in the other months. Observed wind speeds were weaker during the late morning and early afternoon at the upper slope and ridge sites. On the other hand, there was an observed increase in late morning and early afternoon wind speeds at the valley sites. On the contrary, the only diurnal signal present in the COSMO-forecasted winds were late morning/early afternoon increases in wind speed, which were present at all sites.

Another important difference found in the forecast and observational data were differences in the distributions

of wind speeds. Distribution histograms and KSD statistics are shown in Fig. 5. Distribution differences were greatest at the more exposed, higher wind locations. At these locations, especially the ridges, the distributions of forecasted wind speeds had stronger peaks with thinner and shorter tails than the observed distributions. Trends at valley locations were opposite those at the topographically exposed locations—forecast distributions had slightly lower peaks and fatter tails than observations. These stark distribution differences should be a consideration in any downscaling technique applied to these data.

b. Formulation and calibration of downscaling technique

A coherent time series of subdaily forecast data (i.e., 6-h lead times) were only available from November 2014 onward, so the calibration and validation periods focused on the November through June period, except as noted. Based on the prior observations, a downscaling technique was formulated to transpose forecasted winds to the stations. Subgrid terrain structure, hourly forecasted wind speed at the nearest grid cell to each station, and seasonality were included as predictor variables in multi-level linear models of observed bias. The relatively minor wintertime influences of diurnal trends were not included in the downscaling formulation. The linear models were optimized to reduce errors and distribution differences. Multilevel pertains to maintaining the three TPI-defined terrain classes previously described, with separate corrections for each terrain class and each forecast product (COSMO-2 and COSMO-7). Within each TPI terrain class, direction-dependent S_x parameters were included to further describe the subgrid terrain structure. The S_x values were based on hourly station-measured wind directions. To test whether the seasonality could be captured statistically,

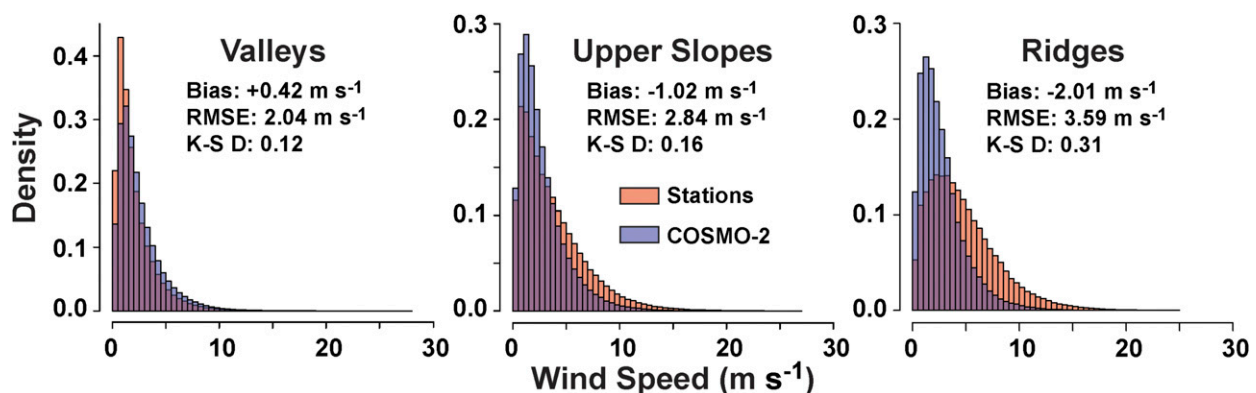


FIG. 5. Histograms of COSMO-2-predicted and observed wind speeds grouped by TPI-defined terrain classes during the validation period.

means and standard deviations (std dev) were derived from all hourly forecast images. During the calibration period, the standard deviations and coefficients of variation (CV; std dev/mean) of the COSMO-2 data had the strongest correlations R with the observed biases at the upper slope (std dev: $R = -0.89$; CV: $R = -0.81$) and ridge sites (std dev: $R = -0.75$; CV: $R = -0.91$). Using a sine function fit, it was found that monthly averaged coefficients of variation over the full 2-yr period including summer months (from September 2013 through August 2015) best captured monthly steps in time ($R^2 = 0.88$, $n = 24$) associated with the trends exhibited in Fig. 4. Monthly standard deviations ($R^2 = 0.70$) and means ($R^2 = 0.32$) were not as effective. Though there was greater scatter fitting the hourly COSMO-2 statistics to a sine function, CVs ($R^2 = 0.24$, $n = 17\,520$) still exhibited a stronger seasonal signal than standard deviations ($R^2 = 0.10$) and means ($R^2 = 0.02$). Hence, CV calculated across the full extent of each hourly COSMO forecast was used to capture the observed seasonality.

The division into three terrain classes with separate corrections for each terrain class and each forecast product produced six classes of corrections. Data within each terrain class contained hourly wind observations from all stations occurring within the TPI-defined terrain class with an observed wind speed greater than 0.2 m s^{-1} and a valid wind direction. Models for each class were fit without a y intercept, and only statistically significant ($p < 0.05$) independent variables were included in the final analysis. Standard error estimates derived from Hessian matrices of the multiparameter model fits were used to determine p values. Furthermore, calibrated coefficients associated with terrain variables were only included if they were physically plausible (e.g., greater wind exposure associated with increasingly negative forecast bias as depicted in Fig. 3 and Table 1).

In summary, the downscaling of COSMO winds to the stations took the following form. For each COSMO product and TPI class,

$$Y_{ij} = \beta_1 X1_{ij} + \beta_2 X2_i + \beta_3 X3_{ij}, \quad (2)$$

where β_1 , β_2 , and β_3 are calibrated coefficients using the optim function [Eq. (3)]; the parameters $X1$, $X2$, and $X3$ are COSMO-forecasted wind speed (m s^{-1}), the CV over the full COSMO domain (dimensionless), and Sx ($^\circ$) based on station location and hourly measured wind direction, respectively; i is all time steps with measured wind speed greater than 0.2 m s^{-1} and a valid wind direction; j is all stations within the TPI group; and $Y_{ij} = X1_{ij} - Z_{ij}$ where Z is the station-observed wind speed (m s^{-1}).

TABLE 3. Calibration period regression results from the dual-optimization fitting of Eq. (2).

	COSMO-2		COSMO-7	
	β	p value	β	p value
Valleys ($n = 653\,125$)				
Forecast speed	0.229	<0.001	0.211	<0.001
CV	-0.055	0.035	0.166	<0.001
Sx-300			0.023	0.004
Upper slopes ($n = 395\,818$)				
Forecast speed	-0.236	<0.001	-0.477	<0.001
CV	0.413	<0.001	1.447	<0.001
Sx-300	0.031	<0.001	0.034	<0.001
Ridges ($n = 92\,724$)				
Forecast speed	-0.464	<0.001	-0.944	<0.001
CV	0.155	0.004	1.444	<0.001
Sx-300	0.033	<0.001	0.034	<0.001

The calibrated coefficients (β_1 , β_2 , and β_3) were determined using the R package optim function that was based on minimizing

$$a \left[\frac{\sqrt{\sum (\hat{Z}_{ij} - Z_{ij})^2}}{n} \right] + b \text{KSD}(\hat{Z}_{ij}, Z_{ij}), \quad (3)$$

where $\hat{Z}_{ij} = X1_{ij} - \hat{Y}_{ij}$; \hat{Y}_{ij} is the estimated COSMO bias from Eq. (2) (m s^{-1}); Z_{ij} is the corrected wind speed (m s^{-1}); KSD(\cdot) is the KSD for the respective distributions; n is the total number of i, j observations; and a, b are the subjectively adjusted weightings. The first term in Eq. (3) represents RMSEs; the second matches the downscaled and observed distributions.

In all cases, forecast wind speeds and CVs were significant model parameters (Table 3) during the calibration period. Sx-300 outperformed the other Sx derivations and was a significant predictor in all classes (after accounting for forecast wind speed and CV), except for the simulation of COSMO-2 biases at the valley sites. Significant fits with the other Sx derivations were also possible at all levels where Sx-300 was significant. It should be noted that in ordinary least squares (OLS) model fits [e.g., $a = 1$ and $b = 0$ in Eq. (3)], terrain parameters, forecast wind speed, and CV were all significant bias predictors in all categories.

Forecast wind speeds were downscaled by class using the dual-optimization model fits [Eq. (2)]. In post-processing, minimum wind values were set at 0.2 m s^{-1} , coinciding with input data stipulations while also ensuring that any subsequent iterative energy flux calculations in the snow model were achieved. The 0.2 m s^{-1} threshold affected less than 2% of the downscaled COSMO-2 winds and $\sim 5\%$ of the downscaled COSMO-7

TABLE 4. Downscaled 1-h results. The numbers in parentheses are the uncorrected results, the nonitalicized numbers without parentheses are the results from downscaling using station-observed wind directions, and the italicized numbers are the results from downscaling using COSMO-predicted wind directions. Downscaling of COSMO-2 valley winds was not direction dependent. Calibration period for both COSMO models and the validation period for COSMO-2 is from November to June; validation period for COSMO-7 is from February to June.

	COSMO-2		COSMO-7	
	Calibration	Validation	Calibration	Validation
RMSE (m s^{-1})				
Overall	(2.62) 2.46	(2.50) 2.33 2.32	(2.67) 2.56	(2.37) 2.30 2.30
Valleys	(2.18) 1.85	(2.04) 1.76	(2.03) 1.79	(1.83) 1.69 1.69
Upper slopes	(3.00) 2.98	(2.84) 2.78 2.78	(3.21) 3.19	(2.78) 2.75 2.75
Ridges	(3.55) 3.49	(3.59) 3.38 3.36	(3.86) 3.84	(3.43) 3.50 3.49
MBE (m s^{-1})				
Overall	(−0.22) −0.10	(−0.29) −0.16 −0.17	(−0.31) −0.17	(−0.31) −0.16 −0.17
Valleys	(0.49) −0.12	(0.42) −0.12	(0.52) −0.17	(0.35) −0.28 −0.28
Upper slopes	(−0.100) −0.11	(−1.02) −0.20 −0.22	(−1.23) −0.21	(−0.99) −0.08 −0.10
Ridges	(−1.92) −0.04	(−2.01) −0.24 −0.26	(−2.29) 0.01	(−1.84) 0.29 0.26
KSD (unitless)				
Overall	(0.04) 0.03	(0.05) 0.03 0.03	(0.10) 0.04	(0.09) 0.05 0.04
Valleys	(0.12) 0.02	(0.12) 0.03	(0.20) 0.05	(0.17) 0.07 0.07
Upper slopes	(0.16) 0.03	(0.16) 0.04 0.05	(0.20) 0.05	(0.18) 0.07 0.07
Ridges	(0.29) 0.04	(0.31) 0.06 0.07	(0.36) 0.02	(0.31) 0.07 0.07

winds. Consistent with the goals of the minimization scheme, biases were greatly reduced and simulated and observed distributions were better matched. All RMSEs during the calibration period were also reduced (Table 4). Relative improvements in the COSMO-2 and COSMO-7 products over the calibration period were quite similar. The percent reductions in RMSEs and absolute MBEs in all TPI classes for the two COSMO products were within 10 percentage points of each other. Only in the overall KSD reductions did the comparative percent reduction between the two COSMO products exceed 10 percentage points, and this was largely due to the uncorrected COSMO-7 KSD value being twice that of the COSMO-2 value. Though the percent reductions were quite similar, RMSEs, MBEs, and KSDs for the downscaled COSMO-2 products generally remained smaller in magnitude than the COSMO-7 downscaled products. This was in large part due to the larger biases and higher KSDs in the original COSMO-7 products (Tables 1, 2).

c. Validation results

The trends in the downscaled validation products relative to the original forecast data were very similar to those from the calibration year. In all but one case RMSEs were slightly reduced, large improvements in bias were achieved in the upper slope and ridge categories, and KSDs were greatly reduced (Table 4). Improvements at the COSMO-2-predicted valley locations were evident as well, though the bias changes were not as substantial as those at the more exposed locations. Comparative interpretations of the COSMO-7 validation

(February–June) and calibration (November–June) results, particularly at the valley sites where larger biases in the forecast data typically occur in the excluded months (Fig. 4), were slightly compromised by the differing time periods analyzed.

The improvements in the simulated distributions can be seen in Figs. 5 and 6. KSDs at the upper slope (ridge) sites have been reduced from 0.16 (0.31) to 0.04 (0.05). The high peaks and thin tails of the original distributions at these sites have been respectively trimmed and filled. Most importantly for this application, the frequencies where high winds were predicted by the downscaled model have substantially increased and were much better matched to the observed frequencies. The intended opposite effects at the valley stations—increasing the peaks and thinning the tails of the simulated distributions—have similarly been achieved with KSD reduced from 0.05 to 0.03. A closer look at bias reductions by TPI (Fig. 7) shows the substantial and consistent bias reductions at the upper slope and ridge sites. Overall, biases were reduced at the valley sites, though these trends were not as consistent as observed at the more exposed sites.

An OLS solution was also applied to demonstrate the consequences of not accounting for distributions in the optimization scheme. Figure 8 shows results from an OLS fit to the calibration dataset applied to the validation year for the COSMO-2 upper slope data. Biases were similarly removed in both the OLS and dual-optimization solutions, and RMSE was lower in the OLS solution (2.52 m s^{-1} compared to 2.84 m s^{-1}). However, distribution differences between the OLS product and

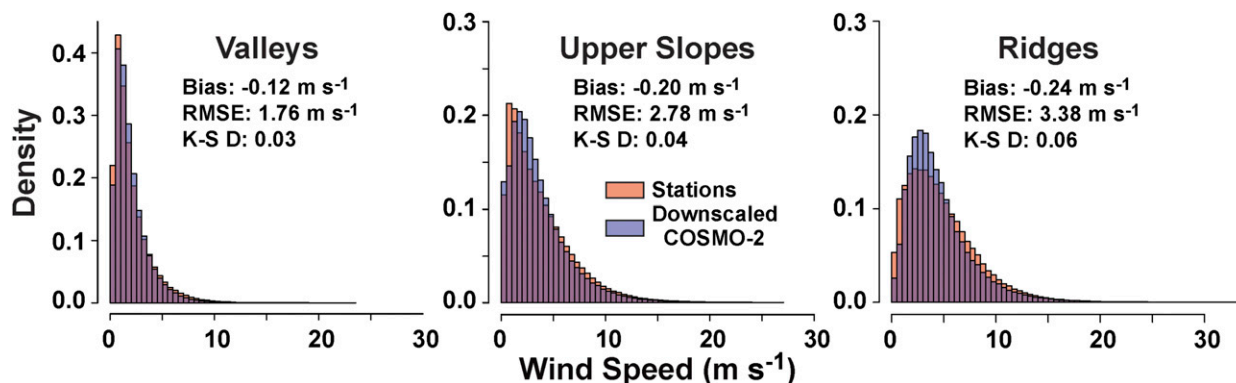


FIG. 6. Histograms of COSMO-2-downscaled and observed wind speeds grouped by TPI-defined terrain classes during the validation period.

observations were even greater than they were between uncorrected COSMO-2 winds and observations (KSD of 0.31 compared to 0.16). Comparing Figs. 5 and 8, one can reach the conclusion that while a correction that disregards distributions may be of benefit in determining long-term means, in all likelihood it will be to the detriment of short-term solutions.

Up to this point, the direction-dependent terrain parameters have been based on observed wind directions. COSMO-predicted wind directions were substituted for the observed directions to test the sensitivity of this approach to errors encountered in a forecast situation when observations are not available. The COSMO-2 corrected valley sites were not affected by this change as the Sx

terrain parameters did not play a role in downscaling at these locations. The results from this analysis indicated that the gains in model performance were not sensitive to potential forecast wind direction errors. RMSEs (greatest decrease in performance was 0.02 m s^{-1}), MBEs (0.02 m s^{-1}), and KSDs (0.01) remained virtually unchanged using the forecasted directions (Table 4).

d. Spatial application

The focus thus far has been on downscaling to specific points; however, the introduced techniques are perfectly suited for spatial downscaling as well. Similar to the station-based application, forecasted wind speeds and directions from COSMO grid cells were assigned to each 25-m-resolution raster cell lying within it. At each 25-m grid cell, Sx was derived from the 25-m-resolution DEM

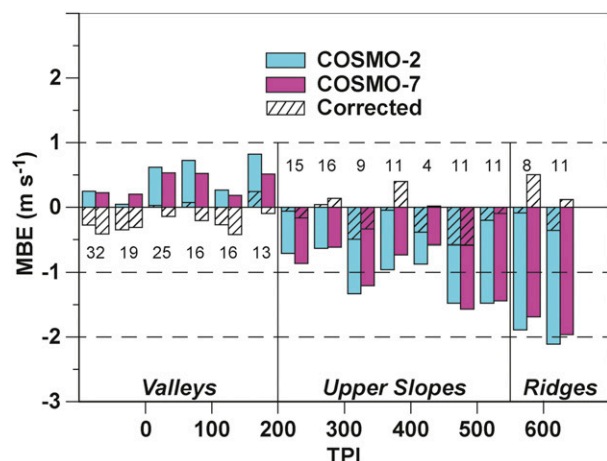


FIG. 7. MBEs binned by TPI for the raw and downscaled COSMO-2 and COSMO-7 products during the validation period. The COSMO-7 validation period was limited to February–June, excluding months with the greatest errors (see Fig. 4). The differing time periods should be considered when making crosswise comparisons to the COSMO-2 results in this figure and with Fig. 3 from the calibration period. The numbers at the base of the bars indicate how many observation sites were in each bin.

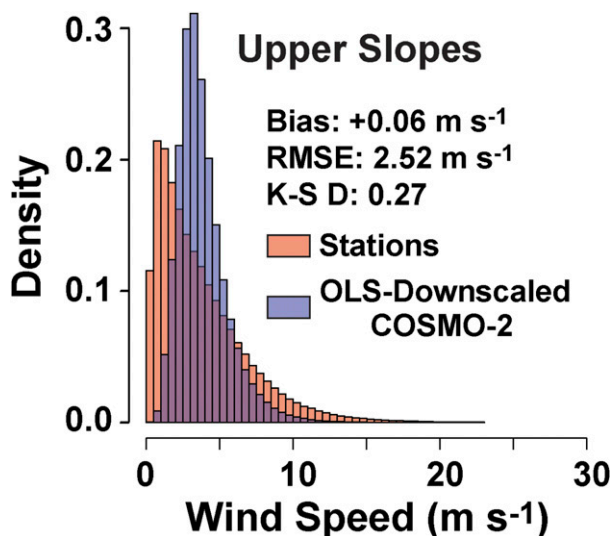


FIG. 8. Histograms of COSMO-2 wind speeds downscaled using an OLS regression and observed wind speeds for the upper slope terrain class during the validation year.

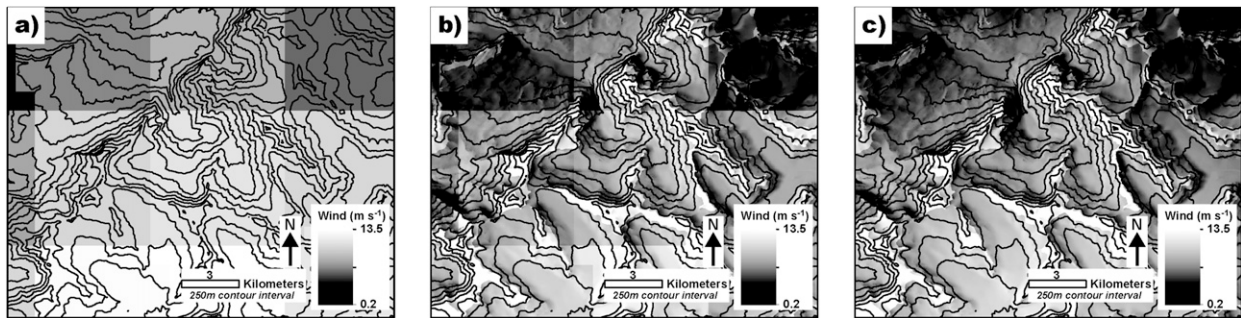


FIG. 9. (a) COSMO-7-forecasted wind field, (b) downscaled using the presented nearest-neighbor point derivations to a 25-m resolution grid, and (c) downscaled using the same approach but to a spatially smoothed COSMO-7 wind field. Winds were primarily out of the west-southwest at this time. Ridge locations exhibit increases in wind speeds after downscaling while differentiations between windward and leeward locations are most obvious on upper slopes.

with upwind terrain defined by COSMO-forecasted wind directions. Likewise, TPI at each 25-m grid cell was based on derivations from the 25-m-resolution DEM. The S_x and TPI values can be calculated in advance and stored in a library facilitating retrievals. CV is taken over the entire extent of the hourly COSMO wind speed forecast. The coefficients in Table 3 are then applied to downscale the COSMO data at each 25-m-resolution grid cell. Figure 9 compares a raw COSMO-7 product (Fig. 9a) with downscaled versions (Figs. 9b,c) when winds were predominantly out of the west-southwest. Figure 9b was based directly on the presented nearest-neighbor methods idealized for point simulations. Artifacts from the original ~ 7 -km-resolution winds remain apparent at the original gridcell boundaries. Figure 9c used the same downscaling methods but first applied a smoothing, low-pass mean filter to the COSMO-7 product to enhance spatial consistency. Spatial coherency can also be a desired outcome, and it is shown here purely for demonstration purposes. Given that the smoothing changes the forecast data input to the downscaling corrections, in practice a recalibration of the coefficients in Table 3 to the smoothed data should be implemented first. The downscaled products both demonstrated higher-resolution, physically plausible details in the wind field that were not resolved in the original product. Ridges exhibited considerably higher wind speeds while windward and leeward differences were accentuated on the upper slopes. The difference between Figs. 9a and 9c demonstrate the potential of this work for downscaling coarser-resolution wind fields to much higher spatial resolutions.

5. Conclusions

This research has shown that even current high-resolution weather models struggle to resolve mountain

winds. This was particularly the case at sites with higher observed wind speeds. Local terrain features, efficiently described by means of digital terrain analysis at much higher resolutions than present in the forecast data, effectively and efficiently delineated spatial biases in the forecast products. Statistical linking of the local terrain with observed forecast biases formed the basis for a downscaling method that effectively removed much of the observed forecast systematic bias. Furthermore, a novel optimization scheme was introduced to ensure that not only were the error metrics improved in the downscaled products, but also that downscaled wind speed distributions were far better matched to the observed distributions. Whereas others have designed downscaling methods to better approximate observations or distributions, to our knowledge this is the first effort to simultaneously achieve both objectives. The diversity and number of wind stations included in this study, incorporation of direction-dependent terrain features in the downscaling methodology, and analysis of hourly data using an independent validation dataset add to the uniqueness of this study. Though analysis focused on downscaling to specific observation sites, it was also demonstrated that these techniques are fully capable of broader spatial applications.

While some of the methodology and certainly the empirically derived coefficients are quite specific to this application, the founding conceptualizations are not. Hence, much of this work should be transferable to other applications. The biases described by the local terrain features match theoretical expectations. Whenever scale mismatches such as these are encountered, similar spatial dependencies are to be expected. All of the terrain parameters used in this study capably delineated the spatial organization of biases, indicating that any method capable of describing local wind conditions could similarly be used. This study obviously

benefited from a vast network of observations. While these observations greatly aided the distribution optimization, the observed distributions were averaged over many sites and can be considered typical of most mountain wind distributions. There is also a large body of research describing wind speed distributions (e.g., Curry et al. 2012; Kirchmeier et al. 2014; Sarkar et al. 2011; van Donk et al. 2005) that can be used to guide optimization schemes in other applications.

The empirically derived regression coefficients were based on tens to hundreds of thousands of observations and produced rather conservative corrections (e.g., 99th percentile hourly COSMO-7 corrections during the calibration period were 3.3 m s^{-1} at upper slope sites and 8.9 m s^{-1} at ridge sites). Observations could certainly be used to guide these coefficients at other sites. An argument can also be made that direct transference would likely still be of benefit in situations where large negative biases are expected, such as when only low-resolution data are available to estimate winds at locally exposed sites. It also bears mentioning that a calibrated model such as this is dependent on the input forecast data remaining stable. Modifications to the weather model, for example, incorporating new assimilation techniques or data, can have nonrandom effects and need to be closely monitored.

The CV was used to characterize seasonal dependencies. While CV was shown to be significantly related to the seasonal patterns, capturing this effect was compromised in the multiparameter, dual-optimization downscaling methodology. Though not shown, a seasonal pattern in downscaled errors was still apparent. Future work will look to more direct approaches of incorporating the seasonal component into the downscaling methodology.

Given the highly complex and stochastic nature of mountain wind fields, a large amount of scatter in predicted and observed wind speeds will most likely always exist. This adds a degree of uncertainty to any modeling effort dependent on wind speeds. Scatter due to stochasticity is natural, and modelers can use techniques such as ensemble modeling to account for this. Systematic biases, however, translate directly through subsequent applications. This research provided a means of identifying and removing many of these biases using an innovative downscaling technique. While this particular downscaling method was designed to work within the time constraints of operational forecasting, benefits should be realized throughout the scientific community.

Acknowledgments. We thank MeteoSwiss for collecting the ANETZ data and making these data available for this study. This study was partly funded by the

Swiss Federal Office for the Environment (FOEN). We also greatly appreciate the work of the two anonymous reviewers who provided very insightful comments that greatly improved this work.

REFERENCES

- Abatzoglou, J. T., 2013: Development of gridded surface meteorological data for ecological applications and modelling. *Int. J. Climatol.*, **33**, 121–131, doi:[10.1002/joc.3413](https://doi.org/10.1002/joc.3413).
- Anderton, S. P., S. M. White, and B. Alvera, 2004: Evaluation of spatial variability in snow water equivalent for a high mountain catchment. *Hydrol. Processes*, **18**, 435–453, doi:[10.1002/hyp.1319](https://doi.org/10.1002/hyp.1319).
- Benestad, R. E., I. Hanssen-Bauer, and D. Chen, 2008: *Empirical–Statistical Downscaling*. World Scientific, 228 pp.
- Curry, C., D. van der Kamp, and A. Monahan, 2012: Statistical downscaling of historical monthly mean winds over a coastal region of complex terrain. I. Predicting wind speed. *Climate Dyn.*, **38**, 1281–1299, doi:[10.1007/s00382-011-1173-3](https://doi.org/10.1007/s00382-011-1173-3).
- Daly, C., M. Halbleib, J. I. Smith, W. P. Gibson, M. K. Doggett, G. H. Taylor, J. Curtis, and P. P. Pasteris, 2008: Physiographically sensitive mapping of climatological temperature and precipitation across the conterminous United States. *Int. J. Climatol.*, **28**, 2031–2064, doi:[10.1002/joc.1688](https://doi.org/10.1002/joc.1688).
- de Rooy, W. C., and K. Kok, 2004: A combined physical–statistical approach for the downscaling of model wind speed. *Wea. Forecasting*, **19**, 485–495, doi:[10.1175/1520-0434\(2004\)019<0485:ACPAFT>2.0.CO;2](https://doi.org/10.1175/1520-0434(2004)019<0485:ACPAFT>2.0.CO;2).
- Erickson, T. A., M. W. Williams, and A. Winstral, 2005: Persistence of topographic controls on the spatial distribution of snow in rugged mountain terrain, Colorado, United States. *Water Resour. Res.*, **41**, W04014, doi:[10.1029/2003WR002973](https://doi.org/10.1029/2003WR002973).
- Etienne, C., A. Lehmann, S. Goyette, J.-I. Lopez-Moreno, and M. Beniston, 2010: Spatial predictions of extreme wind speeds over Switzerland using generalized additive models. *J. Appl. Meteor. Climatol.*, **49**, 1956–1970, doi:[10.1175/2010JAMC2206.1](https://doi.org/10.1175/2010JAMC2206.1).
- Fiddes, J., and S. Gruber, 2014: TopoSCALE v.1.0: Downscaling gridded climate data in complex terrain. *Geosci. Model Dev.*, **7**, 387–405, doi:[10.5194/gmd-7-387-2014](https://doi.org/10.5194/gmd-7-387-2014).
- Freudiger, D., I. Kohn, K. Stahl, and M. Weiler, 2014: Large-scale analysis of changing frequencies of rain-on-snow events with flood-generation potential. *Hydrol. Earth Syst. Sci.*, **18**, 2695–2709, doi:[10.5194/hess-18-2695-2014](https://doi.org/10.5194/hess-18-2695-2014).
- Gao, L., M. Bernhardt, and K. Schulz, 2012: Elevation correction of ERA-Interim temperature data in complex terrain. *Hydrol. Earth Syst. Sci.*, **16**, 4661–4673, doi:[10.5194/hess-16-4661-2012](https://doi.org/10.5194/hess-16-4661-2012).
- Harindra, J., and F. Sermal, 2012: Environmental fluid dynamics. *Handbook of Environmental Fluid Dynamics*, Vol. 1, CRC Press, 3–17.
- Horvath, K., D. Koracin, R. Vellore, J. Jiang, and R. Belu, 2012: Sub-kilometer dynamical downscaling of near-surface winds in complex terrain using WRF and MM5 mesoscale models. *J. Geophys. Res.*, **117**, D11111, doi:[10.1029/2012JD017432](https://doi.org/10.1029/2012JD017432).
- Huang, H.-Y., S. Capps, S.-C. Huang, and A. Hall, 2015: Downscaling near-surface wind over complex terrain using a physically-based statistical modeling approach. *Climate Dyn.*, **44**, 529–542, doi:[10.1007/s00382-014-2137-1](https://doi.org/10.1007/s00382-014-2137-1).
- Jenness, J., 2006: Topographic Position Index extension for ArcView 3.x, v. 1.2. Accessed 6 December 2016. [Available online at <http://www.jennessent.com/arcview/tpi.htm>.]

- Jiménez, P. A., and J. Dudhia, 2012: Improving the representation of resolved and unresolved topographic effects on surface wind in the WRF Model. *J. Appl. Meteor. Climatol.*, **51**, 300–316, doi:[10.1175/JAMC-D-11-084.1](https://doi.org/10.1175/JAMC-D-11-084.1).
- Kattlemann, R., 1997: Flooding from rain-on-snow events in the Sierra Nevada. *IAHS Publ.*, **239**, 59–65.
- Kirchmeier, M. C., D. J. Lorenz, and D. J. Vimont, 2014: Statistical downscaling of daily wind speed variations. *J. Appl. Meteor. Climatol.*, **53**, 660–675, doi:[10.1175/JAMC-D-13-0230.1](https://doi.org/10.1175/JAMC-D-13-0230.1).
- Kumar, M., D. Marks, J. Dozier, M. L. Reba, and A. Winstral, 2013: Evaluation of distributed hydrologic impacts of temperature-index and energy-based snow models. *Adv. Water Resour.*, **56**, 77–89, doi:[10.1016/j.advwatres.2013.03.006](https://doi.org/10.1016/j.advwatres.2013.03.006).
- Lehning, M., H. Löwe, M. Ryser, and N. Raderschall, 2008: Inhomogeneous precipitation distribution and snow transport in steep terrain. *Water Resour. Res.*, **44**, W07404, doi:[10.1029/2007WR006545](https://doi.org/10.1029/2007WR006545).
- Liston, G. E., and M. Sturm, 1998: A snow-transport model for complex terrain. *J. Glaciol.*, **44**, 498–516, doi:[10.3198/1998JG44-148-498-516](https://doi.org/10.3198/1998JG44-148-498-516).
- Marks, D., J. Kimball, D. Tingey, and T. Link, 1998: The sensitivity of snowmelt processes to climate conditions and forest cover during rain-on-snow; a case study of the 1996 Pacific Northwest flood. *Hydrol. Processes*, **12**, 1569–1587, doi:[10.1002/\(SICI\)1099-1085\(199808/09\)12:10<1569::AID-HYP682>3.0.CO;2-L](https://doi.org/10.1002/(SICI)1099-1085(199808/09)12:10<1569::AID-HYP682>3.0.CO;2-L).
- , A. Winstral, and M. Seyfried, 2002: Simulation of terrain and forest shelter effects on patterns of snow deposition, snowmelt and runoff over a semi-arid mountain catchment. *Hydrol. Processes*, **16**, 3605–3626, doi:[10.1002/hyp.1237](https://doi.org/10.1002/hyp.1237).
- Mott, R., M. Schirmer, and M. Lehning, 2011: Scaling properties of wind and snow depth distribution in an Alpine catchment. *J. Geophys. Res.*, **116**, D06106, doi:[10.1029/2010JD014886](https://doi.org/10.1029/2010JD014886).
- Nelder, J. A., and R. Mead, 1965: A simplex method for function minimization. *Comput. J.*, **7**, 308–313, doi:[10.1093/comjnl/7.4.308](https://doi.org/10.1093/comjnl/7.4.308).
- Painter, T. H., and Coauthors, 2016: The Airborne Snow Observatory: Fusion of scanning lidar, imaging spectrometer, and physically-based modeling for mapping snow water equivalent and snow albedo. *Remote Sens. Environ.*, **184**, 139–152, doi:[10.1016/j.rse.2016.06.018](https://doi.org/10.1016/j.rse.2016.06.018).
- Pomeroy, J. W., D. M. Gray, and P. G. Landine, 1993: The Prairie Blowing Snow Model: Characteristics, validation, operation. *J. Hydrol.*, **144**, 165–192, doi:[10.1016/0022-1694\(93\)90171-5](https://doi.org/10.1016/0022-1694(93)90171-5).
- , R. E. Stewart, and P. H. Whitfield, 2016: The 2013 flood event in the South Saskatchewan and Elk River basins: Causes, assessment and damages. *Can. Water Resour. J.*, **41**, 105–117, doi:[10.1080/07011784.2015.1089190](https://doi.org/10.1080/07011784.2015.1089190).
- Purves, R. S., J. S. Barton, W. A. Mackaness, and D. E. Sugden, 1998: The development of a rule-based spatial model of wind transport and deposition of snow. *Ann. Glaciol.*, **26**, 197–202, doi:[10.3198/1998AoG26-1-197-202](https://doi.org/10.3198/1998AoG26-1-197-202).
- Raderschall, N., M. Lehning, and C. Schär, 2008: Fine-scale modeling of the boundary layer wind field over steep topography. *Water Resour. Res.*, **44**, W09425, doi:[10.1029/2007WR006544](https://doi.org/10.1029/2007WR006544).
- R Development Core Team, 2015: R: A language and environment for statistical computing. R Foundation for Statistical Computing, accessed 6 December 2016. [Available online at <https://www.r-project.org/>].
- Running, S. W., R. R. Nemani, and R. D. Hungerford, 1987: Extrapolation of synoptic meteorological data in mountainous terrain and its use for simulating forest evapotranspiration and photosynthesis. *Can. J. For. Res.*, **17**, 472–483, doi:[10.1139/x87-081](https://doi.org/10.1139/x87-081).
- Salameh, T., P. Drobinski, M. Vrac, and P. Naveau, 2009: Statistical downscaling of near-surface wind over complex terrain in southern France. *Meteor. Atmos. Phys.*, **103**, 253–265, doi:[10.1007/s00703-008-0330-7](https://doi.org/10.1007/s00703-008-0330-7).
- Sarkar, A., S. Singh, and D. Mitra, 2011: Wind climate modeling using Weibull and extreme value distribution. *Int. J. Eng. Sci. Technol.*, **3**, 100–106, doi:[10.4314/ijest.v3i5.68571](https://doi.org/10.4314/ijest.v3i5.68571).
- Schirmer, M., V. Wirz, A. Clifton, and M. Lehning, 2011: Persistence in intra-annual snow depth distribution Part 1: Measurements and topographic control. *Water Resour. Res.*, **47**, W09516, doi:[10.1029/2010WR009426](https://doi.org/10.1029/2010WR009426).
- Stuart, B. D., 2012: Laboratory modeling. *Handbook of Environmental Fluid Dynamics*, Vol. 2, CRC Press, 443–456.
- Stull, R. B., 1988: *An Introduction to Boundary Layer Meteorology*. Kluwer Academic Publishers, 666 pp.
- Surfleet, C. G., and D. Tullos, 2013: Variability in effect of climate change on rain-on-snow peak flow events in a temperate climate. *J. Hydrol.*, **479**, 24–34, doi:[10.1016/j.jhydrol.2012.11.021](https://doi.org/10.1016/j.jhydrol.2012.11.021).
- Trubilowicz, J. W., J. M. Shea, G. Jost, and R. D. Moore, 2016: Suitability of North American Regional Reanalysis (NARR) output for hydrologic modelling and analysis in mountainous terrain. *Hydrol. Processes*, **30**, 2332–2347, doi:[10.1002/hyp.10795](https://doi.org/10.1002/hyp.10795).
- van Donk, S. J., L. E. Wagner, E. L. Skidmore, and J. Tartarko, 2005: Comparison of the Weibull model with measured wind speed distributions for stochastic wind generation. *Trans. ASABE*, **48**, 503–510, doi:[10.13031/2013.18324](https://doi.org/10.13031/2013.18324).
- Weiss, A., 2001: Topographic position and landforms analysis. Accessed 6 December 2016. [Available online at www.jennessent.com/downloads/TPI-poster-TNC_18x22.pdf].
- Wever, N., T. Jonas, C. Fierz, and M. Lehning, 2014: Model simulations of the modulating effect of the snow cover in a rain-on-snow event. *Hydrol. Earth Syst. Sci.*, **18**, 4657–4669, doi:[10.5194/hess-18-4657-2014](https://doi.org/10.5194/hess-18-4657-2014).
- Winstral, A., and D. Marks, 2002: Simulating wind fields and snow redistribution using terrain-based parameters to model snow accumulation and melt over a semi-arid mountain catchment. *Hydrol. Processes*, **16**, 3585–3603, doi:[10.1002/hyp.1238](https://doi.org/10.1002/hyp.1238).
- , K. Elder, and R. E. Davis, 2002: Spatial snow modeling of wind-redistributed snow using terrain-based parameters. *J. Hydrometeorol.*, **3**, 524–538, doi:[10.1175/1525-7541\(2002\)003<0524:SSMOWR>2.0.CO;2](https://doi.org/10.1175/1525-7541(2002)003<0524:SSMOWR>2.0.CO;2).
- , D. Marks, and R. Gurney, 2009: An efficient method for distributing wind speeds over heterogeneous terrain. *Hydrol. Processes*, **23**, 2526–2535, doi:[10.1002/hyp.7141](https://doi.org/10.1002/hyp.7141).
- , —, and —, 2013: Simulating wind-affected snow accumulations at catchment to basin scales. *Adv. Water Resour.*, **55**, 64–79, doi:[10.1016/j.advwatres.2012.08.011](https://doi.org/10.1016/j.advwatres.2012.08.011).
- , —, and —, 2014: Assessing the sensitivities of a distributed snow model to forcing data resolution. *J. Hydrometeorol.*, **15**, 1366–1383, doi:[10.1175/JHM-D-13-0169.1](https://doi.org/10.1175/JHM-D-13-0169.1).
- Wood, N., 2000: Wind flow over complex terrain: A historical perspective and the prospect for large-eddy modelling. *Bound.-Layer Meteorol.*, **96**, 11–32, doi:[10.1023/A:1002017732694](https://doi.org/10.1023/A:1002017732694).
- Würzer, S., T. Jonas, N. Wever, and M. Lehning, 2016: Influence of initial snowpack properties on runoff formation during rain-on-snow events. *J. Hydrometeorol.*, **17**, 1801–1815, doi:[10.1175/JHM-D-15-0181.1](https://doi.org/10.1175/JHM-D-15-0181.1).
- Žagar, N., M. Žagar, J. Cedilnik, G. Gregorič, and J. Rakovec, 2006: Validation of mesoscale low-level winds obtained by dynamical downscaling of ERA40 over complex terrain. *Tellus*, **58A**, 445–455, doi:[10.1111/j.1600-0870.2006.00186.x](https://doi.org/10.1111/j.1600-0870.2006.00186.x).